Structure, physical properties, and magnetically tunable topological phases in the topological semimetal EuCuBi

Xuhui Wang [1,2,*] Boxuan Li [1,2,*] Liqin Zhou [1,2] Long Chen [1,2] Yulong Wang,[1,2] Yaling Yang [1,2] Ying Zhou [1,2] Ke Liao [1,2] Hongming Weng [1,2,3,†] and Gang Wang [1,2,3,‡]

[1]*Beijing National Laboratory for Condensed Matter Physics, Institute of Physics, Chinese Academy of Sciences, Beijing 100190, China*
[2]*University of Chinese Academy of Sciences, Beijing 100049, China*
[3]*Songshan Lake Materials Laboratory, Dongguan 523808, China*

A single material achieving multiple topological phases can provide potential application for topological spintronics, whereas the candidate materials are very limited. Here, we report on the structure, physical properties, and possible emergence of multiple topological phases in the recently discovered, air-stable EuCuBi single crystal. EuCuBi crystallizes in hexagonal space group $P6_3/mmc$ (No. 194) in ZrBeSi-type structure with an antiferromagnetic (AFM) ground state below $T_N = 11.2$ K. There is a competition between AFM and ferromagnetic (FM) interactions below T_N revealed by electrical resistivity and magnetic susceptibility measurements. With increasing magnetic field, EuCuBi evolves from the AFM ground state with a small amount of FM component, going through a possible metamagnetic phase, finally reaching the field-induced FM phase. Based on the first-principles calculations, we demonstrate that Dirac and Weyl semimetals, and possibly mirror Chern insulators, can be achieved in EuCuBi by tuning the temperature and applying a magnetic field, making EuCuBi a promising candidate for exploring multiple topological phases.

I. INTRODUCTION

The discovery of topological insulators (TIs) featuring dissipationless gapless edge states has sparked extensive interest in exploring topological states [1–4]. Unlike the gapped bulk states in TIs, topological semimetals have quasiparticles caused by nontrivial band crossings in bulk states [5,6]. Among topological semimetals [7,8], Dirac semimetal (DSM) [5,9–13] and Weyl semimetal (WSM) [5,14–16], in addition to edge states of TIs [17], can create the quasiparticle excitations analogous to relativistic Dirac fermion or Weyl fermion. Triple point semimetal (TPSM) [18–20] with unique surface states [14] and possible topological Lifshitz transitions [21] hosts three-component quasiparticles that do not possess any direct analog of elementary particle in quantum field theory [18]. These quasiparticles emerging from various topological phases can be realized and switched in a single topological magnet by manipulating spin configuration. The tunable topological phases can combine the rich physical properties of quasiparticles and provide a platform for spintronic applications, especially enhancing the efficiency and robustness of spintronic devices due to their exotic electronic states and topological stability against local perturbations [22–24]. Although some topological magnets have been reported, a single material with long-range magnetic order combined with various nontrivial topological electronic structures is highly desired [25–27].

Ternary pnictides with ZrBeSi-type structure having hexagonal space group $P6_3/mmc$ (No. 194) have attracted much attention owing to their rich topological properties. For instance, KHgSb with a honeycomb HgSb layer hosts an hourglass surface state protected by a glide mirror [28,29]. KZnBi was experimentally confirmed to be a three-dimensional (3D) DSM with surface superconductivity [28,29]. Moreover, topological phases in a single ternary pnictide with ZrBeSi-type structure can be tuned. BaAgBi, originally reported as a DSM [30–32], can be tuned into a WSM by Eu doping on the Ba site breaking the time-reversal symmetry or a TPSM by Cu doping on the Ag site breaking the inversion symmetry [32]. Theoretically, SrAgAs can go through multiple topological phase transitions between DSM, TPSM, and TI by controlling the content of doping Cu atoms on the Ag site [18]. However, it is very challenging to experimentally control the occupancy and content of doping atoms for breaking symmetries and inducing topological phases. In contrast, tuning the symmetry by changing the spin configuration in magnetic topological materials is much easier [25,33,34]. For example, EuAgP can be switched between nearly TPSM and WSM by controlling the directions of magnetization [25]. Below the Néel temperature, EuAgAs in an antiferromagnetic (AFM) state is a topological mirror semimetal or TPSM. Above the Néel temperature, it is in a paramagnetic (PM) state with a pair of Dirac points [26]. In addition, EuAgAs was experimentally found to possess the topological Hall effect caused by the nontrivial spin textures of real space [35–39]. Moreover, the introduction of a magnetic atom into topological materials and the enhanced Berry curvature for magnetism result in other properties [40], such as the anomalous Hall effect [41–44], anomalous Nernst

---

*These authors contributed equally to this work.

†hmweng@iphy.ac.cn

‡gangwang@iphy.ac.cn

effect [45–48], magneto-optical effect [49,50], and magnetic spin Hall effect [51–53].

Here, we report on the structure, physical properties, and possibly emerging topological phases of EuCuBi single crystal. As revealed by the electrical resistivity, magnetic susceptibility, and specific heat capacity measurements, EuCuBi undergoes an AFM transition at $T_N = 11.2$ K. Below T_N, the presence of a weak ferromagnetic (FM) component below $\mu_0 H_1$ is probably due to the competition of FM and AFM interactions. By using first-principles calculations, we demonstrate the multiple topological states in EuCuBi and the transition among them. Below T_N and $\mu_0 H_2$, EuCuBi is in the AFM ground state, and the possible magnetic structure is AFM [100] (Néel vector along the *a* axis). For AFM [100], it may be a mirror Chern insulator (MCI) where all intersections of conduction and valence bands are broken. Above $\mu_0 H_3$, spins align ferromagnetically along the direction of applied magnetic field. By shifting the magnetization direction, the magnetic structures of FM [100], FM [110], and FM [001] can be easily obtained, which all host doubly degenerate Weyl points (the spins are aligned along [100] for magnetic structure FM [100]). Under $\mu_0 H_2 < \mu_0 H < \mu_0 H_3$, EuCuBi undergoes a possible metamagnetic (MM) transition and gradually aligning of spins with the magnetic field. Above T_N, EuCuBi is in the PM state as a DSM harbored by a sixfold rotation axis. Combining all the obtained results, the magnetic phase diagram of EuCuBi is established.

II. EXPERIMENTAL DETAILS AND METHODS

A. Single-crystal growth, crystal structure, and chemical composition

The EuCuBi single crystals were grown by the high-temperature solution method using Bi as flux. The europium ingot (99.9%, Alfa Aesar), copper powder (99.9%, Alfa Aesar), and bismuth granules (99.995%, Alfa Aesar) were mixed in a fritted alumina crucible set (Canfield Crucible Set) [54] in a molar ratio of 2:1:4 and then sealed in an fused silica ampoule under vacuum. The sealed ampoule was heated to 1273 K, kept for 24 h, and then slowly cooled down to 923 K at a rate of 3 K/h. At this temperature, the crystals were separated from the remaining flux by centrifugation. Shiny and hexagonal-shaped crystals were obtained with a size up to $1 \times 1 \times 0.5$ mm. The crystal structure was determined by single-crystal x-ray diffraction (SCXRD) on a four-circle diffractometer [Rigaku XtaLAB PRO 007HF(Mo)R-DW, HyPix] at 180 K with multilayer mirror graphite-monochromatized Mo $K\alpha$ radiation ($\lambda = 0.71073$ Å) operated at 50 kV and 40 mA. The x-ray diffraction (XRD) data of the EuCuBi single crystal were measured on a PANalytical X'Pert PRO diffractometer (Cu $K\alpha$ radiation, $\lambda = 1.54178$ Å) operated at 40 kV and 40 mA with a graphite monochromator in a reflection mode ($2\theta = 10° - 100°$, step size = 0.017°). The chemical composition was analyzed by a scanning electron microscope (SEM, Hitachi S-4800) equipped with an electron microprobe analyzer for semiquantitative elemental analysis in energy-dispersive x-ray spectroscopy (EDS) mode.

TABLE I. Crystallographic data and structure refinement for EuCuBi.

Empirical formula	EuCuBi
Formula weight	424.50 g/mol
Space group/Z	$P6_3/mmc$ (No. 194)/2
Unit cell dimensions	$a = 4.6099(1)$ Å, $\alpha = 90°$
	$b = 4.6099(1)$ Å, $\beta = 90°$
	$c = 8.5208(4)$ Å, $\gamma = 120°$
Volume/d_{cal}	156.817(10) Å^3/8.990 g/cm^3
Reflections collected/R(int)	986/0.0789
Data/restraints/parameters	72/0/8
Goodness-of-fit on F^2	1.067
Final R indices [$I > 2\sigma(I)$]	$R_1 = 0.0280$, $\omega R_2 = 0.0761$
R indices (all data)	$R_1 = 0.0291$, $\omega R_2 = 0.0779$
Largest diff. peak and hole	1.919 and -2.077 e Å^{-3}

B. Physical property measurement

Resistivity and magnetoresistance measurements were performed on a physical property measurement system (PPMS, Quantum Design, 7 T). Contacts for standard four-probe configuration were established by attaching platinum wires using silver paint, resulting in a contact resistance $< 5\,\Omega$ with the applied current (~ 2 mA) parallel to the crystallographic *ab* plane and the magnetic field perpendicular to the *ab* plane [55]. Magnetic susceptibility measurements were carried out with applied magnetic field parallel and perpendicular to the *ab* plane using the zero-field-cooling (ZFC) and field-cooling (FC) protocols. Isothermal magnetization data were collected at 2, 4, 6, 8, 12, 20, and 50 K under the applied magnetic field up to 16 T parallel and perpendicular to the *ab* plane on a high-field PPMS (Quantum Design, 16 T). Specific heat capacity data were collected on a PPMS < 220 K.

C. First-principles calculations

The first-principles calculations were carried out using a plane-wave basis set and projector augmented-wave method [56] encoded in VASP [57,58] for the calculation of electronic band structure. The generalized gradient approximation (GGA) parameterized by Perdew, Burke, and Ernzerhof pseudopotential was used for the exchange-correlation functional [59]. We adopted the GGA+Hubbard-U method where $U = 6.0$ eV to deal with the strong correlation effects of the Eu-f electrons in the magnetic phases [60]. The energy of the plane-wave cutoff was set to 500 eV. The convergence criterion for the total energy was set to be 10^{-7} eV. We used a $9 \times 9 \times 7$ *k*-mesh as a sample of the Brillouin zone in the Monkhorst-Pack scheme [60]. All results consider spin-orbit coupling (SOC).

III. RESULTS AND DISCUSSION

A. Crystal structure and magnetotransport

The crystallographic data for EuCuBi determined by SCXRD is shown in Tables I and S1 in the Supplemental Material [61]. EuCuBi crystallizes in the hexagonal space group $P6_3/mmc$ (No. 194) having the ZrBeSi-type structure with $a = 4.6099(1)$ Å, $b = 4.6099(1)$ Å, $c = 8.5208(4)$ Å,
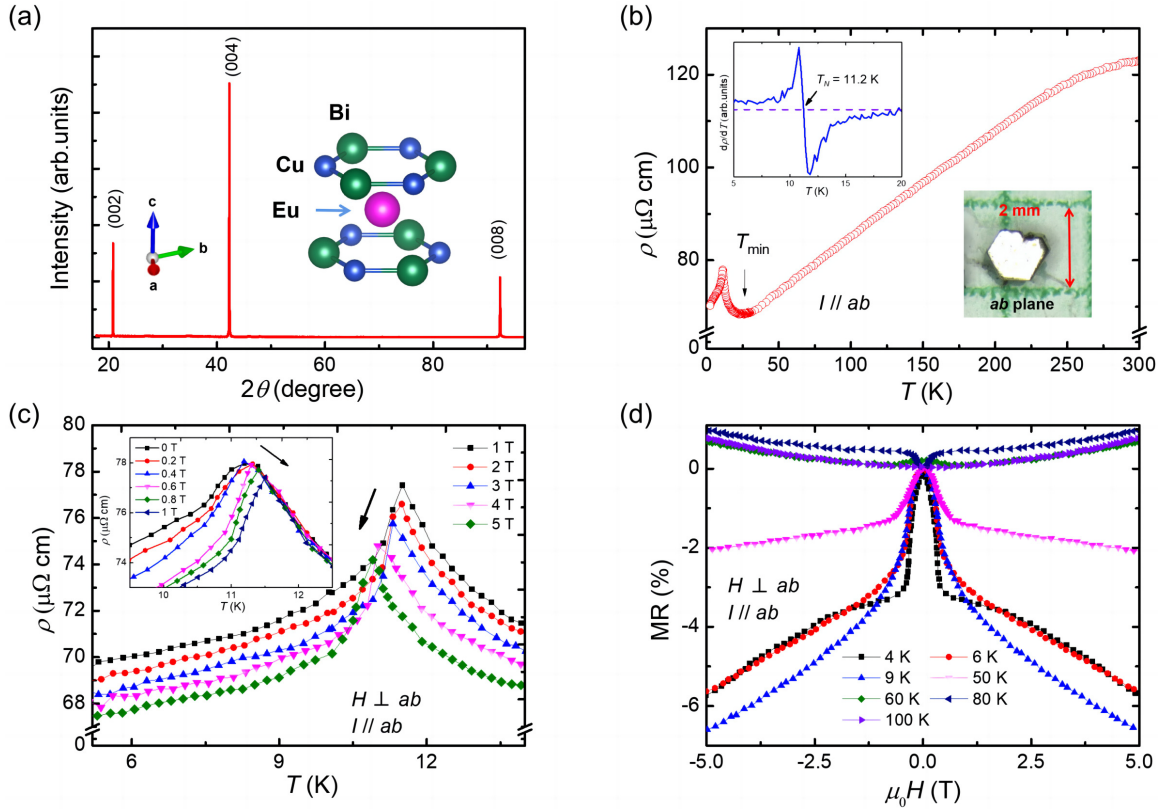
FIG. 1. (a) X-ray diffraction (XRD) pattern of EuCuBi single crystal. The inset shows the schematic crystal structure of EuCuBi. (b) Temperature dependence of resistivity for $I//ab$. The upper inset shows the derivative of ρ ($d\rho/dT$). The lower inset shows the optical photograph of EuCuBi single crystal. (c) Temperature-dependent resistivity for $H\perp ab$ (1–5 T and $<$ 1 T in the inset) and $I//ab$. (d) Transverse magnetoresistance (TMR) at different temperatures up to 100 K.

$\alpha = \beta = 90°$, and $\gamma = 120°$. The Cu and Bi atoms are alternately arranged to form a honeycomb layer in AB stacking along the c axis. The Eu atoms are located between the neighboring CuBi layers. The XRD pattern of EuCuBi single crystal is shown in Fig. 1(a), where only the $(00l)$ ($l =$ even) diffraction peaks are observed, indicating that the hexagonal-shaped plane is the crystallographic ab plane.

The temperature-dependent electrical resistivity of the EuCuBi single crystal measured in the temperature range of 2–300 K with the current being parallel to the ab plane ($I//ab$) is shown in Fig. 1(b). It has a residual resistivity ratio (RRR; $\rho_{300\,K}/\rho_{T\,min}$) of $\sim$ 1.79 [see Fig. 1(b)], close to those of EuAgAs (RRR $= 1.96$) [39], EuAuAs (RRR $= 2.07$) [64], and EuCuAs (RRR $= 1.35$) [65]. The resistivity at 300 K is 122.97 $\mu\Omega$ cm, which is comparable with those of EuAgAs (100 $\mu\Omega$ cm) [39], EuCuAs (110 $\mu\Omega$ cm) [65], and SrAuAs (126 $\mu\Omega$ cm) [66] but lower than that of EuAuAs (430 $\mu\Omega$ cm) [64]. The resistivity gradually decreases with decreasing temperature above $T_{min} = 24$ K, exhibiting a metalliclike behavior. Below T_{min}, the resistivity first increases and then decreases, exhibiting a sharp anomaly at $T_N = 11.2$ K. The decrease in resistivity below T_N is due to the reduced carrier scattering for ordered Eu^{2+} moments.

By applying magnetic field perpendicular to the ab plane ($H\perp ab$), this anomaly is gradually suppressed with the magnetic field increasing from 1 to 5 T, exhibiting the low-temperature shifting and intensity decrease [Fig. 1(c)]. This

behavior is typical for an AFM transition [67]. Notably, below the magnetic field of 1 T, the anomaly moves toward higher temperature as the magnetic field increases [the inset of Fig. 1(c)], showing a behavior of FM transition [68–70]. Thus, there probably is competition between FM and AFM interactions [71,72].

The magnetic-field-dependent transverse magnetoresistance (TMR) defined by $[\rho(H) - \rho(0)]/\rho(0) \times 100\%$ at different temperatures is shown in Fig. 1(d) ($I//ab$, $H\perp ab$). TMR is negative with a cusplike feature due to the suppression of magnetic fluctuation by increased applied magnetic field $<$ 50 K (well above $T_N = 11.2$ K) and becomes positive $>$ 50 K. This suggests that the magnetic fluctuation exists well above T_N. Under a magnetic field of 5 T, TMR reaches -5.73% at 4 K, -6.63% at 9 K, and being $<$ 1% at 100 K. The absolute value of TMR at 9 K is larger than that at 4 K, like that of EuAgAs [39], which may be due to the larger magnetic fluctuation close to T_N resulting in more significant magnetic field suppression.

B. Magnetic properties

Figures 2(a) and 2(b) show the ZFC magnetic susceptibility and its inversion for the EuCuBi single crystal with a magnetic field of 0.1 T parallel ($\chi_{//}$) and perpendicular ($\chi_\perp$) to the ab plane at temperatures ranging from 2–300 K, respectively. Here, $\chi_{//}$ shows a sharper peak at 11.2 K than $\chi_\perp$ at 11 K, suggesting that the magnetic moments
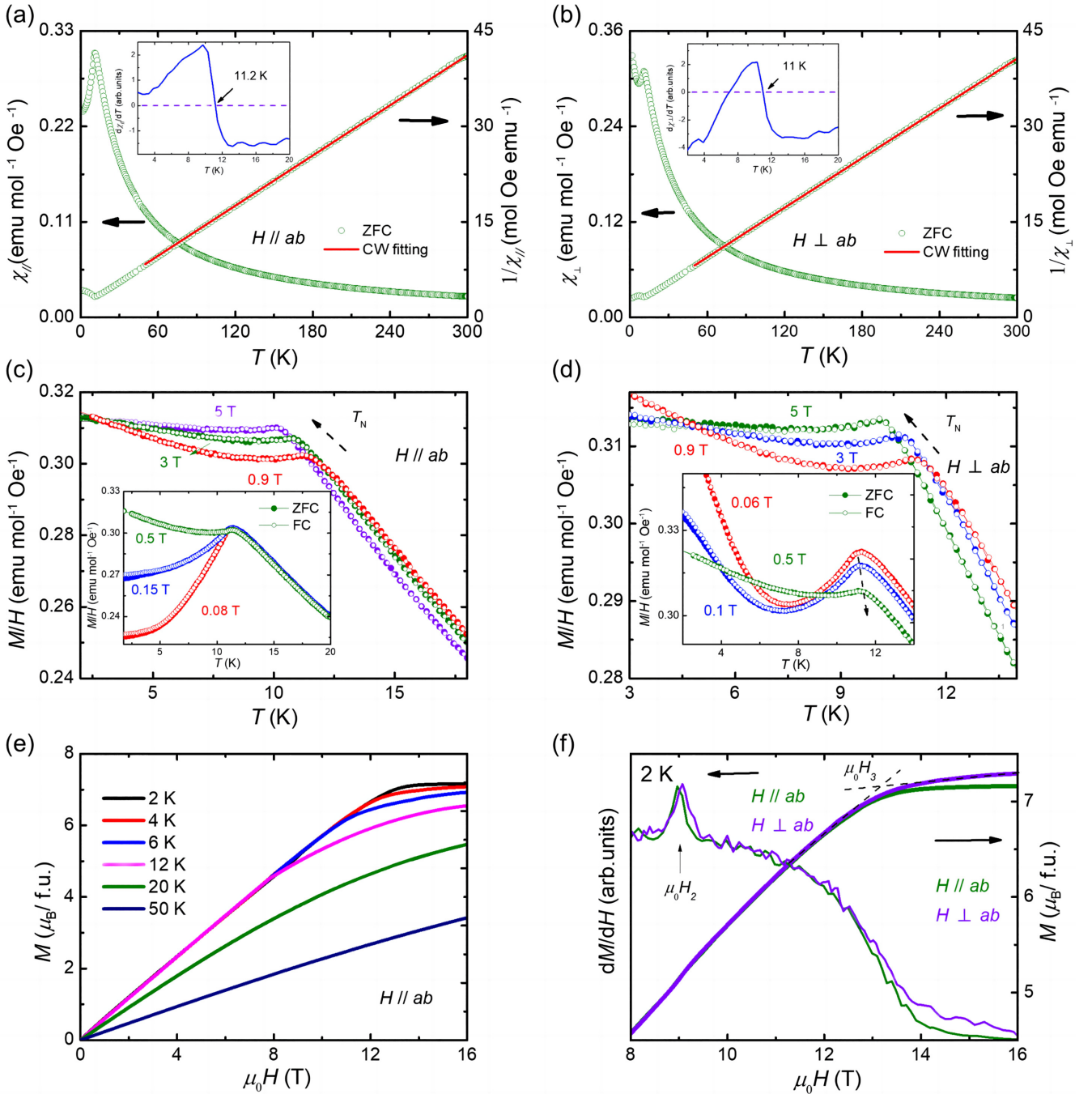
FIG. 2. Temperature dependence of magnetic susceptibility for EuCuBi single crystal for (a) $H//ab$ and (b) $H \perp ab$. The red solid lines show the Curie-Weiss fittings. Magnetic susceptibility vs T measured in zero-field-cooled (ZFC; filled circle) and field-cooled (FC; hollow circle) protocols for (c) $H//ab$ and (d) $H \perp ab$ ($0.9 \text{ T} < \mu_0 H_1$). The insets of (c) and (d) show the magnetic susceptibility under magnetic field < 1 T. (e) Magnetic field dependence of isothermal magnetization up to 16 T for EuCuBi single crystal at different temperatures for $H//ab$. (f) Isothermal magnetization and the derivative of magnetization (dM/dH) for $H//ab$ and $H \perp ab$ at 2 K.

align in the ab plane [65,73,74]. The extended Curie-Weiss law $\chi(T) = C/(T - \Theta_P) + \chi_0$, where χ_0 is the temperature-independent susceptibility, C the Curie constant, and Θ_p the PM Weiss temperature, is used to fit the magnetic susceptibility at high temperature. The parameters and the effective magnetic moment derived by the fitting are listed in Table II. The estimated effective magnetic moments are 7.71 μ_B/f.u. for $H//ab$ and 7.77 μ_B/f.u. for $H \perp ab$. Both

are close to the theoretical value $g\sqrt{S(S+1)}\mu_B = 7.94 \, \mu_B$ with $g = 2$ and $S = \frac{7}{2}$ for free Eu^{2+}. The obtained Weiss temperature Θ_p is negative, -10.99 and -11.17 K for $H//ab$ and $H \perp ab$, respectively. This indicates the predominance of AFM interaction among Eu^{2+} moments. Additionally, there is almost no difference between $\chi_{//}$ and $\chi_\perp > 50$ K, indicating that the susceptibility of EuCuBi is quite isotropic in the high-temperature range.

TABLE II. Fitting parameters for the magnetic susceptibility of EuCuBi single crystal at temperatures ranging from 50 to 300 K using the extended Curie-Weiss law.

Parameter	$H//ab$	$H \perp ab$
χ_0 ($\times 10^{-4}$ emu/mol Oe)	3.94	4.22
C (emu K/mol Oe)	7.43	7.54
Θ_p (K)	-10.99	-11.17
μ_{eff} (μ_B/f.u.)	7.71	7.77

Figures 2(c) and 2(d) show the ZFC and FC curves under certain magnetic fields parallel and perpendicular to the ab plane, respectively. Around T_N, $\chi_{//}$ increases and then decreases rapidly with decreasing temperature, forming a distinct peak associated with the AFM transition under low magnetic field [the inset of Fig. 2(c)], whereas for $\chi_\perp$, it exhibits a nonmonotonic behavior below $\mu_0 H_1$ (Fig. S2 in the Supplemental Material [61]), which first decreases and then increases as the temperature drops [the inset of Fig. 2(d)]. This behavior also implies the competition between FM and AFM interactions, like that of EuAgAs [39]. Above $\mu_0 H_1$, both $\chi_{//}$ and $\chi_\perp$ have magnetic transitions that shift to lower temperature with increasing magnetic field [Figs. 2(c) and 2(d)], which corresponds to the AFM order. Below $\mu_0 H_1$, $d\chi_{//}/dT$ vs T and $d\chi_\perp/dT$ vs T both have peaks that shift toward higher temperature with increasing magnetic field in common with the FM order (Figs. S2(c) and S2(d) in the Supplemental Material [61]). This is coincident with resistivity and susceptibility under low magnetic field. The hysteresis loop can be seen in $M(H)$ curves for $H//ab$ and $H \perp ab$, again supporting the existence of a FM component (Figs. S2(a) and S2(b) in the Supplemental Material [61]).

Isothermal magnetization was measured in both directions ($H//ab$ and $H \perp ab$), as shown in Figs. 2(e) and 2(f). At 2 K, the magnetization increases almost linearly and then gradually saturates to 7.15 and 7.29 μ_B/f.u. for $H//ab$ and $H \perp ab$, respectively, with FM-like spin alignment along the direction of applied magnetic field. Both saturated values are a little bit larger than the theoretical saturated magnetic moment $gS\mu_B = 7\,\mu_B$ for Eu^{2+}. Despite small magnetocrystalline anisotropy (consistent with theoretical results below), the easy axis of magnetization should lie in the ab plane. At 50 K, the magnetization shows linear magnetic field dependence in the whole measured magnetic field range. Notably, dM/dH vs H curves have a peak ~ 9 T corresponding to the kink of M-H curves, which exhibit small hysteresis ~ 9 T for $H//ab$ and $H \perp ab$ (Figs. S3(a) and S3(b) in the Supplemental

Material [61]). This suggests that a MM transition is underway. As the magnetization is clearly not saturated up to $\mu_0 H_3$ [see Fig. 2(f)], magnetic moments continue to rotate toward the magnetic field above $\mu_0 H_2$.

The isostructural compounds, like EuAgAs [39,75], EuCuAs [65], and EuAuAs [64], all have A-type AFM order, in which Eu^{2+} is in the FM alignment within the ab plane and in the AFM alignment along the c axis Table III. Considering the very similar magnetic susceptibility and small magnetic anisotropy, EuCuBi most probably also has A-type AFM order.

C. Heat capacity

The specific heat capacity $C_P(T)$ of the EuCuBi single crystal was measured under zero field in the temperature range of 2–213 K and is shown in Fig. 3(a). A distinct λ-shaped peak is observed ~ 11.2 K, which is consistent with $\chi(T)$ and $\rho(T)$. The value of $C_P(T)$ at 213 K is 67.6 J/mol K, which is close to the classical Dulong-Petit limit $C_P = 3NR = 74.83$ J/mol K with $N = 3$ for EuCuBi, where N is the number of atoms per formula unit, R the ideal gas constant. The $C_P(T)$ in the temperature range 18–213 K was fitted by the Debye model using the expression as follows:

$$C_D(T) = 9NR\left(\frac{T}{\theta_D}\right)^3 \int_0^{\theta_D/T} \frac{x^4 e^x}{(e^x - 1)^2} dx, \quad (1)$$

$$C_P(T) = \gamma T + C_D, \quad (2)$$

where Θ_D is the Debye temperature, γ the Sommerfeld coefficient, and γT the electron specific heat term. As shown by the dashed line in Fig. 3(a), the fitting has obvious deviation in the high-temperature region and yields an unphysically negative γ. The Debye model assumes that no lattice vibration mode exists above the Debye frequency ω_D. This leads to an overestimation of the contribution of low-frequency vibrations (below ω_D) to specific heat capacity. As the Einstein model only considers a vibration frequency ω_E, the inclusion of it can complement a small amount of contribution of vibrations with frequencies above ω_D to specific heat capacity. A much better fitting is obtained by combining the Debye model with the Einstein model using the expression as follows [64,76]:

$$C_E(T) = 3NR\left(\frac{\theta_E}{T}\right)^2 \frac{e^{\theta_E/T}}{(e^{\theta_E/T} - 1)^2}, \quad (3)$$

$$C_P(T) = \gamma T + (1 - b)C_E + bC_D, \quad (4)$$

TABLE III. Summary of the magnetic properties and inferred magnetic structure from experimental and theoretical results of several materials with ZrBeSi-type structure [39,64,65].

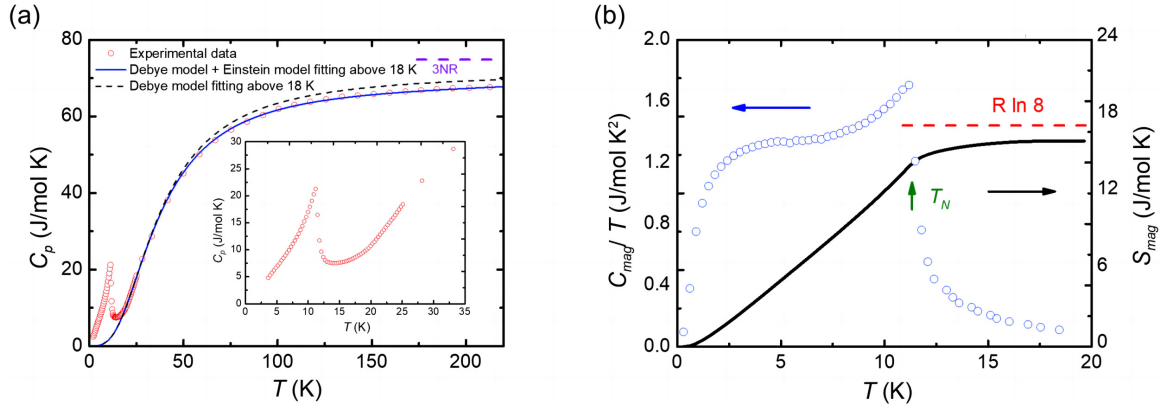| Materials	Magnetic ground state	AFM and FM competition	T_N (K)	Θ_p (K) $H//ab$	Θ_p (K) $H \perp ab$	Magnetic structure (A-type AFM)	Ref.
EuCuAs	AFM		14	19.7	18.4	Spins within ab plane	[65]
EuAgAs	AFM	√	12	10.4	8.7	AFM [110]	[39]
EuAuAs	AFM		6	6.7	4.1	AFM [001]	[64]
EuCuBi	AFM	√	11.2	-10.99	-11.17	AFM [100]	This paper

FIG. 3. (a) Temperature dependence of specific heat capacity of EuCuBi single crystal, which is fitted by the Debye model and the sum of Debye and Einstein models. The inset displays the zoomed magnetic transition peak. (b) C_{mag}/T vs T of EuCuBi single crystal (blue hollow circle) and the calculated magnetic entropy S_{mag} vs T shown by the solid line.

where Θ_E is the Einstein temperature, and b is the weighting factor determining the weight of the Debye model in the lattice specific heat capacity. The parameters obtained from this fitting are as follows: $\gamma = 3.12\,\mathrm{mJ/mol\,K^2}$, $\Theta_D = 151$ K, $\Theta_E = 400$ K, and $b = 0.92$. The Einstein temperature 400 K is higher than that of EuAuAs ($\Theta_E = 313$ K) and EuMg$_2$Bi$_2$ ($\Theta_E = 305$ K), which may be correlated to the high-frequency optical modes [64,76]. In addition, we also fitted $C_P(T)$ in the temperature range of 50–213 K by Eq. (4) and extrapolated it to low temperature (Fig. S4(a) in the Supplemental Material [61]). As shown in Fig. S4(b) in the Supplemental Material [61], there is a deviation between two temperature ranges of fitting, which may come from the magnon contributions of Eu^{2+}. The magnetic part of specific heat capacity $C_{\mathrm{mag}}(T)$ is obtained by subtracting the fitting curve obtained using Eq. (4) from the sum of the Debye and Einstein models. The $S_{\mathrm{mag}}(T)$ is derived by the expression:

$$S_{\mathrm{mag}} = \int_0^T \frac{C_{\mathrm{mag}}}{T} dT, \tag{5}$$

As shown in Fig. 3(b), $S_{\mathrm{mag}}(T)$ tends to saturate and is close to the theoretical value $R\ln(2S+1) = 17.3$ J/mol K for $S = \frac{7}{2}$ at higher temperature. At T_N, S_{mag} achieves a value of 16.09 J/mol K and reaches 85.5% of $R\ln(8)$ J/mol K. In view of the classical λ-shaped specific heat peak, the corresponding transition should belong to the typical second-order magnetic transition [77–79].

D. Phase diagram

Combining the results presented above, the magnetic phase diagram of EuCuBi is summarized in Fig. 4. The transition temperatures obtained from the magnetic susceptibility are determined by $d\chi/dT$. The critical magnetic fields are determined by dM/dH from the magnetization. More details can be seen in the Supplemental Material [61]. There are five regions in the magnetic phase diagram: below T_N and $\mu_0 H_2$, spins align AFM; above $\mu_0 H_3$, spins align FM along the applied magnetic field direction; when $\mu_0 H_2 < \mu_0 H < \mu_0 H_3$, spins undergo the possible MM transition and continue rotation toward the magnetic field; and in the low-field region above

T_N, EuCuBi is in the PM state. A weak FM component may exist in the region below T_N and $\mu_0 H_1$.

E. Electronic structure

Within the unit cell of EuCuBi, Eu is at the Wyckoff position of $2a$, Cu at the position of $2d$, and Bi at the position of $2c$. It is noticed that this structure contains a C_6 rotation axis and a vertical σ_v mirror plane, which protect the crossing points on the high-symmetry axis. The degeneracy points near the Fermi energy mainly come from the s orbitals of Cu and Bi and d orbitals of Eu, whereas the magnetism comes from the f orbitals of Eu.

To figure out the possible magnetic configurations of EuCuBi below T_N, the total energies of three probable AFM spin configurations, AFM [001], AFM [100], and AFM [110], were calculated. As shown in Fig. 5(c), the total energy of AFM [100] is the lowest, showing the magnetic moments align in the ab plane, but the energy difference between AFM [100] and AFM [001] is very small (33 μeV), also indicating small magnetocrystalline anisotropy. For the self-consistent
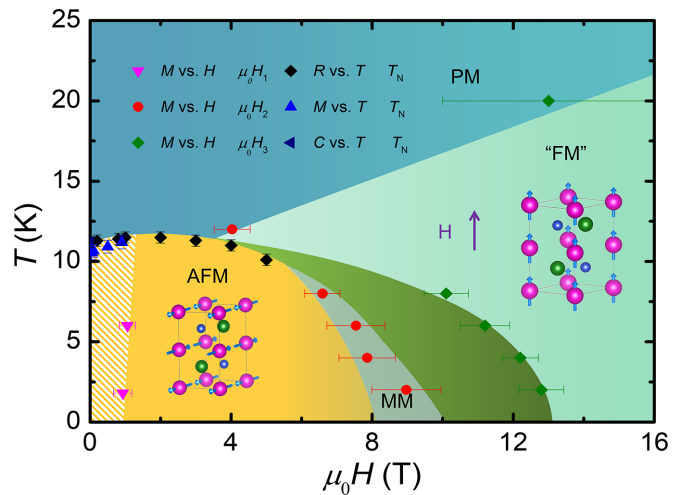

FIG. 4. Magnetic phase diagram for EuCuBi with $H \perp ab$. The possible magnetic phases are shown in the corresponding regions. Different symbols indicate critical temperatures determined by different measurements.
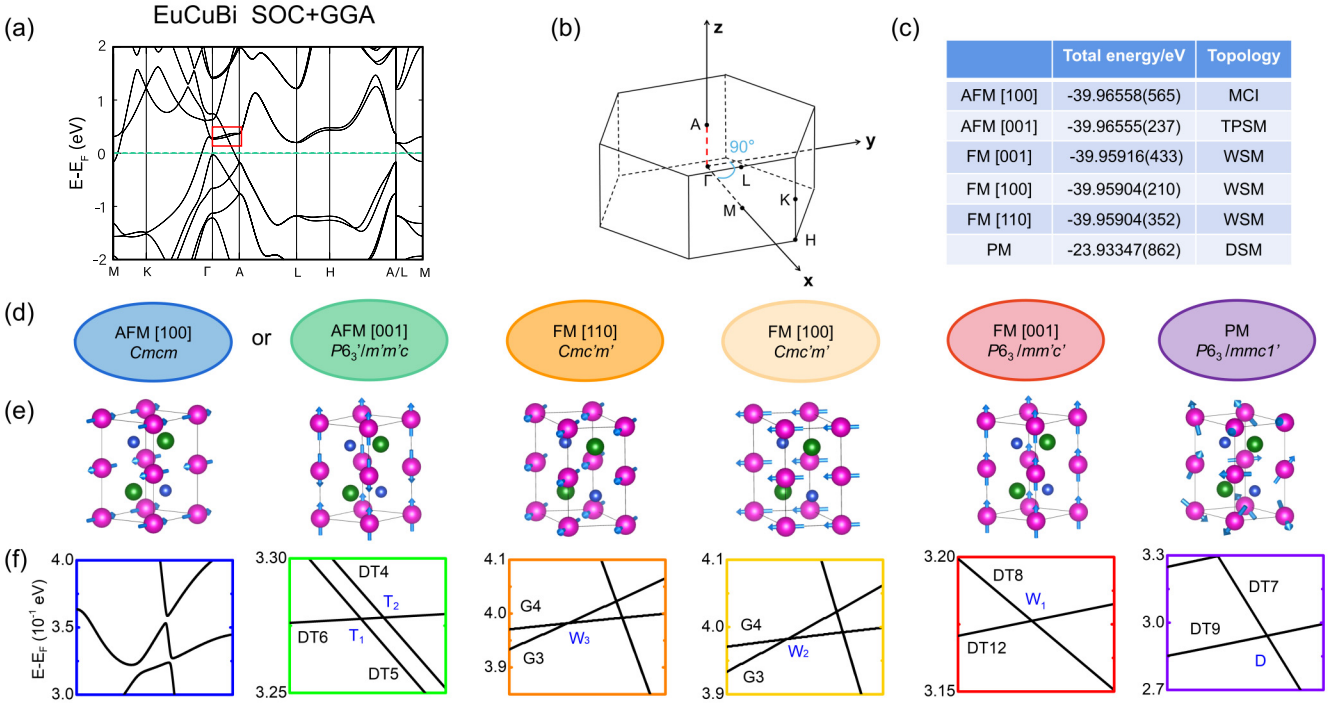
FIG. 5. (a) Calculated band structure of the paramagnetic (PM) phase with spin-orbit coupling (SOC). (b) Bulk Brillouin zone (BZ) of EuCuBi. (c) Total energy and topological features of different magnetic phases. (d) Magnetic space groups of the different accessible phases. (e) Schematic of the spin configurations. (f) Effect of different magnetic structures on the band structure along the Γ-A path.

calculation, AFM [110] is hard to converge, so the convergence criterion for its electronic energy is set to be 10^{-6} eV, while all the numerical tolerance for other configurations is set to be 10^{-7} eV. We also calculated the total energy of three probable FM configurations: FM [100], FM [110], and FM [001]. Among them, the total energy of FM [001] is the lowest but still higher than that of AFM [100], further indicating the AFM state is energetically favorable as the ground state. Above T_N, EuCuBi is in the PM state. The spin configurations of FM [001], [100], and [110] can be obtained by applying magnetic field along the [001], [100], and [110] directions until the magnetization reaches saturation at which the spins align along the magnetic field direction.

We then calculated the topological features of different magnetic configurations for EuCuBi. The calculated band structure along the Γ-A path is shown in Fig. 5(f). For PM EuCuBi, the conduction and valence bands intersect at point D. Since both time-reversal and inversion symmetries are preserved in the PM state, all bands are doubly degenerate. The magnetic little cogroup of the Γ-A path is $6/m'mm$, and the conduction and valence bands belong to the two-dimensional irreducible corepresentations DT7 and DT9, respectively. Point D is a fourfold degenerate Dirac point protected by C_6 symmetry. Next, we considered the band structure of the AFM [001] configuration. The Dirac point is broken for the absence of time-reversal symmetry. The doubly degenerate band and the two nondegenerate bands intersect and form two triple degenerate points T_1 and T_2. The double degenerate band belongs to the irreducible corepresentation DT6 of the magnetic little group, while the other two bands belong to DT4 and DT5, respectively. For the AFM [100] configuration, the intersections between the conduction and valence bands

are all destroyed. Since we find the nontrivial mirror Chern number for the mirror M_z, the AFM [100] phase of EuCuBi is a possible MCI (see more detail on MCIs in the Supplemental Material [61]). In addition, the band structure of the FM [001] configuration is shown in Fig. 5(f). Its magnetic little cogroup of the Γ-A path is $62'2'$, in which there are only one-dimensional (1D) irreducible representations. The nondegenerate conduction and valence bands intersect at the W_1 point, forming a doubly degenerate Weyl point protected by C_6 symmetry. Finally, the magnetic little cogroup of the Γ-A path in FM [100] and FM [110] configurations is $m'm2'$. The conduction and valence bands belong to 1D irreducible corepresentations G4 and G3, respectively, and they intersect at points W_2 and W_3, forming doubly degenerate Weyl points.

IV. CONCLUSIONS

In summary, EuCuBi crystallizes in the hexagonal $P6_3/mmc$ space group with honeycomb layers formed by Bi and Cu atoms, in which the sixfold rotation axis protects the degenerate points on the Γ-A path. An AFM transition at $T_N = 11.2$ K is confirmed by the resistivity, magnetization, and specific heat capacity measurements. The presence of a weak FM component below T_N and $\mu_0 H_1$ suggests that there is competition between FM and AFM interactions. A magnetic phase diagram of EuCuBi is established. Below T_N, the symmetries influenced by the long-range magnetic order lead to the emergence of multiple topological states, including TPSM, WSM, and possible MCI. The magnetic phases with different topological states can be effectively obtained by tuning the magnetic field and temperature. Magnetic tuned topological phase transitions may provide a perspective on spintronics. The results indicate that EuCuBi should be a

promising candidate for revealing the interplay of topology and magnetism and exploring applications of spintronics.

ACKNOWLEDGMENTS

[1] M. Z. Hasan and C. L. Kane, Rev. Mod. Phys. **82**, 3045 (2010).

[2] J. E. Moore, Nature (London) **464**, 194 (2010).

[3] X.-L. Qi and S.-C. Zhang, Rev. Mod. Phys. **83**, 1057 (2011).

[4] P. Wang, J. Ge, J. Li, Y. Liu, Y. Xu, and J. Wang, The Innovation **2**, 100098 (2021).

[5] N. P. Armitage, E. J. Mele, and A. Vishwanath, Rev. Mod. Phys. **90**, 015001 (2018).

[6] C.-K. Chiu, J. C. Y. Teo, A. P. Schnyder, and S. Ryu, Rev. Mod. Phys. **88**, 035005 (2016).

[7] A. Bernevig, H. Weng, Z. Fang, and X. Dai, J. Phys. Soc. Jpn. **87**, 041001 (2018).

[8] H. Weng, X. Dai, and Z. Fang, J. Phys.: Condens. Matter **28**, 303001 (2016).

[9] B. J. Wieder, Y. Kim, A. M. Rappe, and C. L. Kane, Phys. Rev. Lett. **116**, 186402 (2016).

[10] S. M. Young, S. Zaheer, J. C. Y. Teo, C. L. Kane, E. J. Mele, and A. M. Rappe, Phys. Rev. Lett. **108**, 140405 (2012).

[11] S. Mardanya, B. Singh, S.-M. Huang, T.-R. Chang, C. Su, H. Lin, A. Agarwal, and A. Bansil, Phys. Rev. Mater. **3**, 071201(R) (2019).

[12] Z. Wang, Y. Sun, X.-Q. Chen, C. Franchini, G. Xu, H. Weng, X. Dai, and Z. Fang, Phys. Rev. B **85**, 195320 (2012).

[13] P. Liu, A. Zhang, J. Han, and Q. Liu, The Innovation **3**, 100343 (2022).

[14] B. Bradlyn, J. Cano, Z. Wang, M. G. Vergniory, C. Felser, R. J. Cava, and B. A. Bernevig, Science **353**, aaf5037 (2016).

[15] A. A. Soluyanov, D. Gresch, Z. Wang, Q. Wu, M. Troyer, X. Dai, and B. A. Bernevig, Nature (London) **527**, 495 (2015).

[16] H. Weng, C. Fang, Z. Fang, B. A. Bernevig, and X. Dai, Phys. Rev. X **5**, 011029 (2015).

[17] Y. L. Chen, J. G. Analytis, J.-H. Chu, Z. K. Liu, S.-K. Mo, X. L. Qi, H. J. Zhang, D. H. Lu, X. Dai, Z. Fang *et al.*, Science **325**, 178 (2009).

[18] C. Mondal, C. K. Barman, A. Alam, and B. Pathak, Phys. Rev. B **99**, 205112 (2019).

[19] C. K. Barman, C. Mondal, B. Pathak, and A. Alam, Phys. Rev. B **99**, 045144 (2019).

[20] H. Weng, C. Fang, Z. Fang, and X. Dai, Phys. Rev. B **93**, 241202(R) (2016).

[21] Z. Zhu, G. W. Winkler, Q. S. Wu, J. Li, and A. A. Soluyanov, Phys. Rev. X **6**, 031003 (2016).

[22] J.-P. Hanke, F. Freimuth, C. Niu, S. Blügel, and Y. Mokrousov, Nat. Commun. **8**, 1479 (2017).

[23] Y. Fan, P. Upadhyaya, X. Kou, M. Lang, S. Takei, Z. Wang, J. Tang, L. He, L. T. Chang, M. Montazeri *et al.*, Nat. Mater. **13**, 699 (2014).

[24] L. Smejkal, J. Zelezny, J. Sinova, and T. Jungwirth, Phys. Rev. Lett. **118**, 106402 (2017).

[25] L. M. Schoop, A. Topp, J. Lippmann, F. Orlandi, L. Muchler, M. G. Vergniory, Y. Sun, A. W. Rost, V. Duppel, M. Krivenkov *et al.*, Sci. Adv. **4**, eaar2317 (2018).

[26] Y. Xu, Z. Song, Z. Wang, H. Weng, and X. Dai, Phys. Rev. Lett. **122**, 256402 (2019).

[27] Y. Hu, C. Yue, D. Yuan, J. Gao, Z. Huang, Z. Fang, C. Fang, H. Weng, and W. Zhang, Sci. China: Phys., Mech. Astron. **65**, 297211 (2022).

[28] J. Ma, C. Yi, B. Lv, Z. Wang, S. Nie, L. Wang, L. Kong, Y. Huang, P. Richard, P. Zhang *et al.*, Sci. Adv. **3**, e1602415 (2017).

[29] Z. Wang, A. Alexandradinata, R. J. Cava, and B. A. Bernevig, Nature (London) **532**, 189 (2016).

[30] Y. Chang, X. Wang, S. Na, and W. Zhang, Front. Chem. **9**, 796323 (2021).

[31] Q. D. Gibson, L. M. Schoop, L. Muechler, L. S. Xie, M. Hirschberger, N. P. Ong, R. Car, and R. J. Cava, Phys. Rev. B **91**, 205128 (2015).

[32] C. K. Barman, C. Mondal, B. Pathak, and A. Alam, Phys. Rev. Mater. **4**, 084201 (2020).

[33] H. Chen, J. Gao, L. Chen, G. Wang, H. Li, Y. Wang, J. Liu, J. Wang, D. Geng, Q. Zhang *et al.*, Adv. Mater. **34**, e2110664 (2022).

[34] S. Nie, Y. Sun, F. B. Prinz, Z. Wang, H. Weng, Z. Fang, and X. Dai, Phys. Rev. Lett. **124**, 076403 (2020).

[35] N. Kanazawa, Y. Onose, T. Arima, D. Okuyama, K. Ohoyama, S. Wakimoto, K. Kakurai, S. Ishiwata, and Y. Tokura, Phys. Rev. Lett. **106**, 156603 (2011).

[36] A. Neubauer, C. Pfleiderer, B. Binz, A. Rosch, R. Ritz, P. G. Niklowitz, and P. Boni, Phys. Rev. Lett. **102**, 186602 (2009).

[37] W. Wang, M. W. Daniels, Z. Liao, Y. Zhao, J. Wang, G. Koster, G. Rijnders, C. Z. Chang, D. Xiao, and W. Wu, Nat. Mater. **18**, 1054 (2019).

[38] W. Wang, Y. Zhang, G. Xu, L. Peng, B. Ding, Y. Wang, Z. Hou, X. Zhang, X. Li, E. Liu *et al.*, Adv. Mater. **28**, 6887 (2016).

[39] A. Laha, R. Singha, S. Mardanya, B. Singh, A. Agarwal, P. Mandal, and Z. Hossain, Phys. Rev. B **103**, L241112 (2021).

[40] S. Nakatsuji and R. Arita, Annu. Rev. Condens. Matter Phys. **13**, 119 (2022).

[41] N. Kiyohara, T. Tomita, and S. Nakatsuji, Phys. Rev. Appl. **5**, 064009 (2016).

[42] K. Kuroda, T. Tomita, M. T. Suzuki, C. Bareille, A. A. Nugroho, P. Goswami, M. Ochi, M. Ikhlas, M. Nakayama, S. Akebi *et al.*, Nat. Mater. **16**, 1090 (2017).

[43] S. Nakatsuji, N. Kiyohara, and T. Higo, Nature (London) **527**, 212 (2015).

[44] A. K. Nayak, J. E. Fischer, Y. Sun, B. Yan, J. Karel, A. C. Komarek, C. Shekhar, N. Kumar, W. Schnelle, J. Kubler *et al.*, Sci. Adv. **2**, e1501870 (2016).

[45] S. N. Guin, P. Vir, Y. Zhang, N. Kumar, S. J. Watzman, C. Fu, E. Liu, K. Manna, W. Schnelle, J. Gooth *et al.*, Adv. Mater. **31**, e1806622 (2019).

[46] M. Ikhlas, T. Tomita, T. Koretsune, M.-T. Suzuki, D. Nishio-Hamane, R. Arita, Y. Otani, and S. Nakatsuji, Nat. Phys. **13**, 1085 (2017).

[47] A. Sakai, S. Minami, T. Koretsune, T. Chen, T. Higo, Y. Wang, T. Nomoto, M. Hirayama, S. Miwa, D. Nishio-Hamane *et al.*, Nature (London) **581**, 53 (2020).

[48] A. Sakai, Y. P. Mizuta, A. A. Nugroho, R. Sihombing, T. Koretsune, M.-T. Suzuki, N. Takemori, R. Ishii, D. Nishio-Hamane, R. Arita *et al.*, Nat. Phys. **14**, 1119 (2018).

[49] T. Higo, H. Man, D. B. Gopman, L. Wu, T. Koretsune, E. Van, Y. P. Kabanov, D. Rees, Y. Li, and M. T. Suzuki, Nat. Photonics **12**, 73 (2018).

[50] M. Wu, H. Isshiki, T. Chen, T. Higo, and Y. C. Otani, Appl. Phys. Lett. **116**, 132408 (2020).

[51] M. Kimata, H. Chen, K. Kondou, S. Sugimoto, P. K. Muduli, M. Ikhlas, Y. Omori, T. Tomita, A. H. MacDonald, S. Nakatsuji *et al.*, Nature (London) **565**, 627 (2019).

[52] T. Nan, C. X. Quintela, J. Irwin, G. Gurung, D. F. Shao, J. Gibbons, N. Campbell, K. Song, S. Choi, L. Guo *et al.*, Nat. Commun. **11**, 4671 (2020).

[53] J. Zelezny, Y. Zhang, C. Felser, and B. Yan, Phys. Rev. Lett. **119**, 187204 (2017).

[54] P. C. Canfield, T. Kong, U. S. Kaluarachchi, and N. H. Jo, Philos. Mag. **96**, 84 (2015).

[55] Y. Zhou, L. Chen, G. Wang, Y.-X. Wang, Z.-C. Wang, C.-C. Chai, Z.-N. Guo, J.-P. Hu, and X.-L. Chen, Chin. Phys. Lett. **39**, 047401 (2022).

[56] P. E. Blöchl, Phys. Rev. B **50**, 17953 (1994).

[57] G. Kresse and J. Furthmüller, Phys. Rev. B **54**, 11169 (1996).

[58] G. Kresse and D. Joubert, Phys. Rev. B **59**, 1758 (1999).

[59] J. P. Perdew, K. Burke, and M. Ernzerhof, Phys. Rev. Lett. **77**, 3865 (1996).

[60] S. L. Dudarev, G. A. Botton, S. Y. Savrasov, C. J. Humphreys, and A. P. Sutton, Phys. Rev. B **57**, 1505 (1998).

[61] See Supplemental Material at http://link.aps.org/supplemental/10.1103/PhysRevB.108.115126 for atomic coordinates and equivalent isotropic displacement parameters for EuCuBi; the chemical composition analyzed by SEM in EDS mode; isothermal magnetization of EuCuBi single crystal and the derivative of magnetization and magnetic susceptibility; fitting for specific heat capacity data from 18 to 213 K by the sum of the Debye and Einstein models and comparison with fitting > 50 K; some details about calculated topological properties; and brief introduction to mirror Chern insulators. The Supplemental Material also contains Refs. [62,63].

[62] Y. Ando and L. Fu, Annu. Rev. Condens. Matter Phys. **6**, 361 (2015).

[63] T. Zhang, Y. Jiang, Z. Song, H. Huang, Y. He, Z. Fang, H. Weng, and C. Fang, Nature (London) **566**, 475 (2019).

[64] S. Malick, J. Singh, A. Laha, V. Kanchana, Z. Hossain, and D. Kaczorowski, Phys. Rev. B **105**, 045103 (2022).

[65] J. Tong, J. Parry, Q. Tao, G.-H. Cao, Z.-A. Xu, and H. Zeng, J. Alloys Compd. **602**, 26 (2014).

[66] S. Xu, H. Wang, Y.-Y. Wang, Y. Su, X.-Y. Wang, and T.-L. Xia, J. Cryst. Growth **531**, 125304 (2020).

[67] A. Laha and Z. Hossain, J. Magn. Magn. Mater. **465**, 654 (2018).

[68] Y. Zhou, L. Xing, G. J. Finkelstein, X. Gui, M. G. Marshall, P. Dera, R. Jin, and W. Xie, Inorg. Chem. **57**, 14298 (2018).

[69] X.-Q. Zheng and B.-G. Shen, Chin. Phys. B **26**, 027501 (2017).

[70] Q. Y. Dong, J. Chen, X. Q. Zhang, X. Q. Zheng, J. R. Sun, and B. G. Shen, J. Appl. Phys. **114**, 173911 (2013).

[71] B. K. Cho, P. C. Canfield, and D. C. Johnston, Phys. Rev. B **53**, 8499 (1996).

[72] J. E. Ortmann, J. Y. Liu, J. Hu, M. Zhu, J. Peng, M. Matsuda, X. Ke, and Z. Q. Mao, Sci. Rep. **3**, 2950 (2013).

[73] H. Masuda, H. Sakai, M. Tokunaga, Y. Yamasaki, A. Miyake, J. Shiogai, S. Nakamura, S. Awaji, A. Tsukazaki, H. Nakao *et al.*, Sci. Adv. **2**, e1501117 (2016).

[74] S. Jiang, S. Luo, Z. Ren, Z. Zhu, C. Wang, X. Xu, Q. Tao, G. Cao, and Z. Xu, New J. Phys. **11**, 025007 (2009).

[75] Y. Jin, X.-T. Zeng, X. Feng, X. Du, W. Wu, X.-L. Sheng, Z.-M. Yu, Z. Zhu, and S. A. Yang, Phys. Rev. B **104**, 165424 (2021).

[76] S. Pakhira, M. A. Tanatar, and D. C. Johnston, Phys. Rev. B **101**, 214407 (2020).

[77] L. Li, O. Niehaus, M. Kersting, and R. Pöttgen, Intermetallics **62**, 17 (2015).

[78] U. B. Paramanik, P. L. Paulose, S. Ramakrishnan, A. K. Nigam, C. Geibel, and Z. Hossain, Supercond. Sci. Technol. **27**, 075012 (2014).

[79] A. A. Trofimov, X. Hu, H. Wang, Y. Yang, and K. A. Terrani, J. Nucl. Mater. **542**, 152569 (2020).